LETTER

doi:10.1038/nature13966

MapZ marks the division sites and positions FtsZ rings in *Streptococcus pneumoniae*

Aurore Fleurie[1]*, Christian Lesterlin[2]*, Sylvie Manuse[1]*, Chao Zhao[1]†, Caroline Cluzel[3], Jean-Pierre Lavergne[1], Mirita Franz-Wachtel[4], Boris Macek[4], Christophe Combet[1], Erkin Kuru[5], Michael S. VanNieuwenhze[5], Yves V. Brun[5], David Sherratt[2] & Christophe Grangeasse[1]

In every living organism, cell division requires accurate identification of the division site and placement of the division machinery. In bacteria, this process is traditionally considered to begin with the polymerization of the highly conserved tubulin-like protein FtsZ into a ring that locates precisely at mid-cell[1]. Over the past decades, several systems have been reported to regulate the spatiotemporal assembly and placement of the FtsZ ring[2–5]. However, the human pathogen *Streptococcus pneumoniae*, in common with many other organisms, is devoid of these canonical systems and the mechanisms of positioning the division machinery remain unknown[4,6]. Here we characterize a novel factor that locates at the division site before FtsZ and guides septum positioning in pneumococcus. Mid-cell-anchored protein Z (MapZ) forms ring structures at the cell equator and moves apart as the cell elongates, therefore behaving as a permanent beacon of division sites. MapZ then positions the FtsZ ring through direct protein–protein interactions. MapZ-mediated control differs from previously described systems mostly on the basis of negative regulation of FtsZ assembly. Furthermore, MapZ is an endogenous target of the Ser/Thr kinase StkP, which was recently shown to have a central role in cytokinesis and morphogenesis of *S. pneumoniae*[7–9]. We show that both phosphorylated and non-phosphorylated forms of MapZ are required for proper Z-ring formation and dynamics. Altogether, this work uncovers a new mechanism for bacterial cell division that is regulated by phosphorylation and illustrates that nature has evolved a diversity of cell division mechanisms adapted to the different bacterial clades.

Recently, some membrane Hanks-type Ser/Thr kinases[10,11] were shown to have a key role in bacterial cell division and morphogenesis[12]. *S. pneumoniae* StkP kinase is crucial for septum assembly, cell shape and localization of peptidoglycan (PG) synthesis[7–9]. However, the underlying regulatory mechanisms by which StkP exerts its function remain elusive. Here, we uncover the role of one endogenous target of StkP, Spr0334, a membrane protein of unknown function that shares no sequence similarity with other known proteins[13]. We named the protein MapZ for mid-cell-anchored protein Z, on the basis of the observations we report here.

In pneumococcus, the *mapZ*-null mutant (Δ*mapZ*) exhibits a variety of aberrant cell shapes and sizes that contrast with wild-type cell morphology (Fig. 1a and Extended Data Fig. 1a). Misshaped Δ*mapZ* cells have mispositioned division septa and form grape-like clusters as observed by electron microscopy (Fig. 1b). These phenotypes are associated with growth defects, as indicated by a 48% increase in generation time and a 30% decrease in cell viability (Extended Data Table 1). Normal cell shape, viability and growth were restored when *mapZ* was reinserted into the chromosome (*mapZ*$^+$) or complemented from an ectopic chromosome locus (Δ*mapZ*/P_{Zn}-*mapZ*) (Extended Data Fig. 1 and Extended Data Table 1). Bioinformatics analysis[14] of the MapZ sequence predicted the presence of a single transmembrane segment separating a cytoplasmic amino-terminal domain and an extracellular carboxy-terminal domain (Fig. 1c and Extended Data Fig. 2a). Wide-field microscopy showed that MapZ fused to green fluorescent protein (GFP–MapZ; N-terminal fusion) forms rings positioned at mid-cell and at future division sites (Fig. 1c). Consistent with domain prediction, no fluorescence was detected for MapZ–GFP (extracellular C-terminal fusion) (Extended Data Fig. 2b). The C-terminal extracellular domain is required for MapZ septal localization, as its deletion results in redistribution of MapZ all over the cell

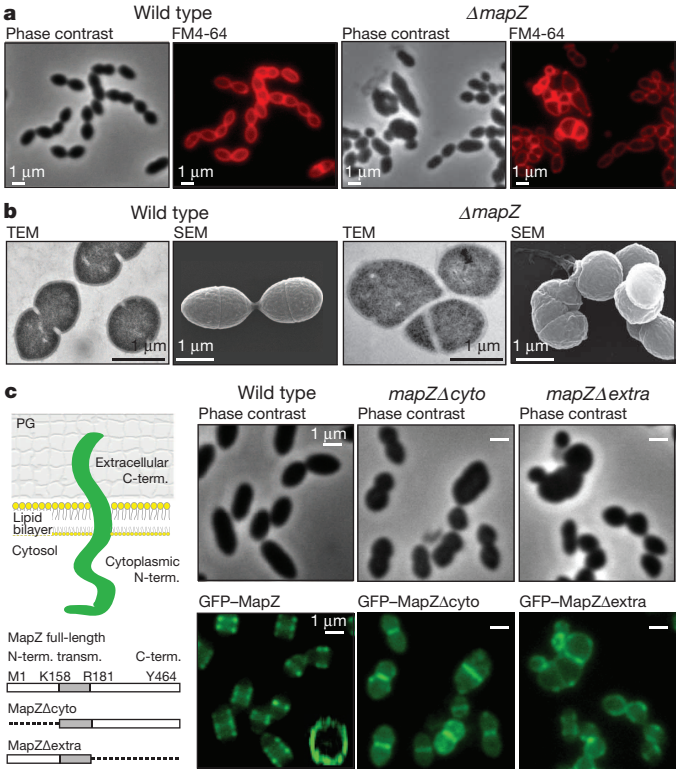


Figure 1 | Characterization of MapZ. **a**, Cell shape was observed by phase contrast microscopy and after membrane staining with FM4-64. **b**, Transmission electron microscopy (TEM) and scanning electron microscopy (SEM). **c**, Diagram of MapZ domain prediction using TOPCONS (http://topcons.net; see Methods), with an intracellular N-terminal domain (N-term.), a transmembrane domain (Transm.) and an extracellular C-terminal domain (C-term.). Wide-field microscopy images show the localization of GFP–MapZ full-length and GFP–MapZΔcyto and GFP–MapZΔextra, in which the N-terminal or the C-terminal domain are deleted, respectively. Images are representative of experiments made in triplicate.

[1]Bases Moléculaires et Structurales des Systèmes Infectieux, IBCP, Université Lyon 1, CNRS, UMR 5086, Lyon 69007, France. [2]Department of Biochemistry, University of Oxford, South Parks Road, Oxford OX1 3QU, UK. [3]Laboratoire de Biologie Tissulaire et d'Ingénierie Thérapeutique, IBCP, Université Lyon 1, CNRS, UMR 5305, Lyon 69007, France. [4]Proteome Center Tübingen, University of Tübingen, Auf der Morgenstelle 15, Tübingen 72076, Germany. [5]Departments of Biology and Chemistry, Indiana University, Bloomington, Indiana 47405, USA. †Present address: Key laboratory of Medical Molecular Virology, School of Basic Medical Sciences, Shanghai Medical College, Fudan University, Shanghai 200032, China.
*These authors contributed equally to this work.

©2014 Macmillan Publishers Limited. All rights reserved

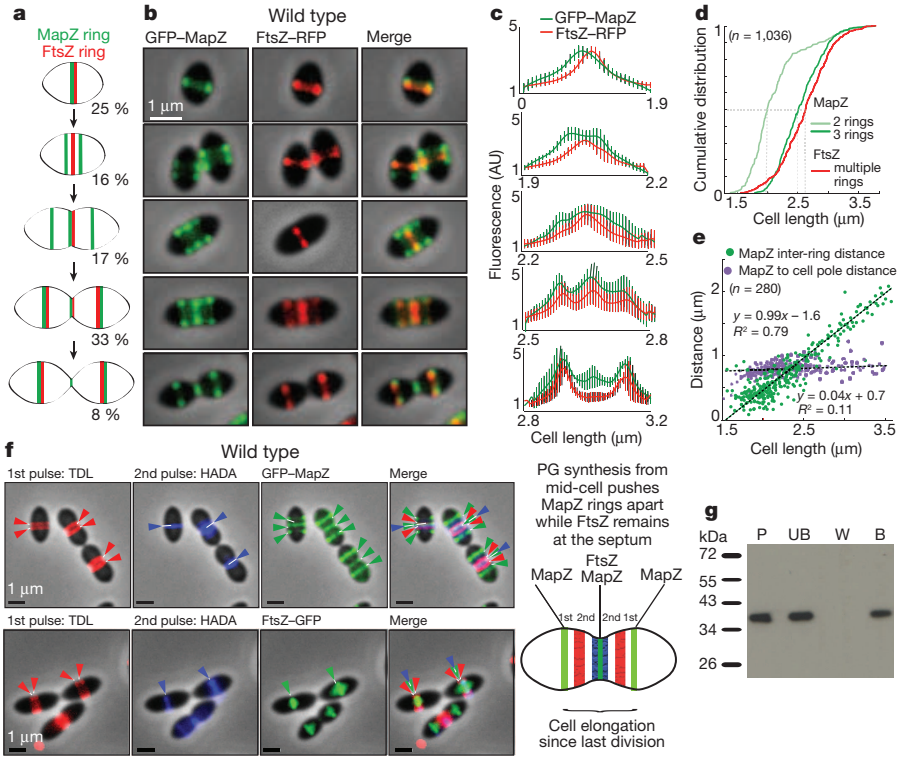


Figure 2 | Localization of MapZ and FtsZ in wild-type cells. **a**, MapZ- and FtsZ-ring positions during growth (with corresponding cell ratios) **b**, Microscopy of GFP–MapZ and FtsZ fused to red fluorescent protein (FtsZ–RFP). **c**, Fluorescence intensities for different cell size categories (error bars show standard deviation (s.d.) for 10 cells analysed). AU, arbitrary units. **d**, Cumulative distribution of cells with MapZ or FtsZ rings. Dashed lines show cumulative distribution of 0.5. **e**, Distance between outer MapZ rings and between MapZ rings and the closest pole. Linear fitting curve with equation and R^2 values are shown. **f**, Localization of consecutive PG incorporation, TDL (a fluorescent carboxytetramethylrhodamine derivative of D-alanine) (red) and HADA (a fluorescent hydroxy coumarin derivative of D-alanine) (blue), together with GFP–MapZ or FtsZ–GFP. Summary diagram is presented. **g**, Interaction of MapZ extracellular domain with the cell wall (sample of *n* cells analysed). Images are representative of experiments made in triplicate. B, MapZ bound; P, purified MapZ alone; UB, unbound; W, wash fraction.

membrane, whereas GFP–MapZΔcyto mostly retained septum localization (Fig. 1c). However, both the intra- and the extracellular domains are required for MapZ cellular function because *mapZΔextra* and *mapZΔcyto* strains exhibit morphological and growth defects similar to Δ*mapZ* (Fig. 1c, Extended Data Fig. 1 and Extended Data Table 1).

In newborn wild-type cells, the MapZ ring and FtsZ ring colocalize at mid-cell (Fig. 2a–c). As cells begin elongating, the MapZ ring splits into two rings whereas a single FtsZ ring remains at mid-cell. At an average cell size of 1.95 μm, 50% of cells have two MapZ rings while >90% of cells still have one single FtsZ ring (Fig. 2d). The early and progressive splitting of MapZ was observed in detail by time-lapse (Extended Data Fig. 4a and Supplementary Video 1) and three-dimensional structured illumination (3D-SIM) snapshot microscopy (Extended Data Fig. 4b–d). At a later stage (average cell size of 2.5 μm), the appearance of a third MapZ ring at mid-cell is shortly followed by splitting of FtsZ into rings that migrate apart until colocalization with MapZ outer rings at future

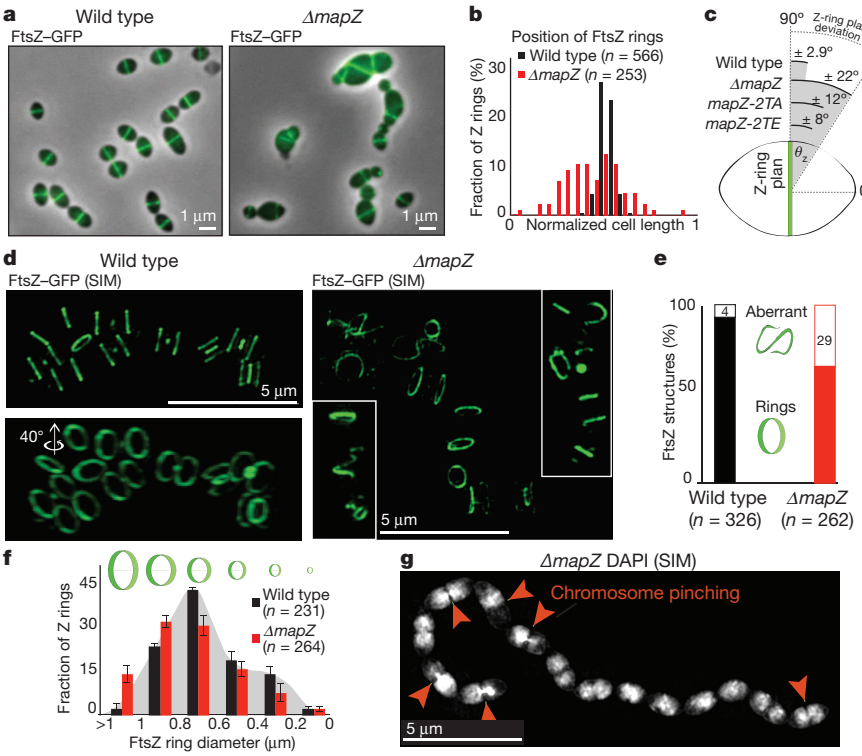


Figure 3 | FtsZ localization in wild-type and Δ*mapZ* cells. **a**, Localization of FtsZ–GFP. **b**, Positioning of single FtsZ rings. **c**, Deviation of FtsZ-ring angles (θ_z) (60 cells analysed for each strain; *P* value $< 2.9 \times 10^{-2}$). **d**, 3D-SIM of FtsZ rings. **e**, Fraction of FtsZ rings or aberrant structures (*P* value $= 1.4 \times 10^{-10}$, two-tailed Student's *t*-test). **f**, FtsZ-ring diameter distribution (error bars show s.d. from three independent experiments; *P* value $= 1.1 \times 10^{-3}$). **g**, 3D-SIM of Δ*mapZ* cells after DNA staining with DAPI (sample of *n* cells analysed). Images are representative of experiments made in triplicate.

©2014 Macmillan Publishers Limited. All rights reserved

division sites (Fig. 2a–d and Extended Data Fig. 3a, b). The mid-cell MapZ/FtsZ ring constricts and eventually closes (Fig. 2a–c and Extended Data Fig. 3a–c) to complete cytokinesis. Identical MapZ and FtsZ localizations were observed in the *rfp-mapZ ftsZ-gfp* strain (Extended Data Fig. 3e).

Importantly, the distance between the outer MapZ rings increases linearly as a function of the cell length, whereas the distance between MapZ and the cell pole remains constant (Fig. 2e). This suggested that MapZ rings are permanently associated with the future division sites and are mechanically pushed apart as PG synthesis forms the new cell halves. This hypothesis was confirmed by visualizing GFP–MapZ together with PG synthesis using sequential incorporation of two fluorescently labelled D-amino acids[15] (Methods). Consistent with a previous report[16], our results showed that PG is incorporated at mid-cell (Fig. 2f). The last synthetized PG (Fig. 2f, blue) pushes the previously incorporated one (Fig. 2f, red) and both are flanked by MapZ rings, while a single FtsZ ring is present at mid-cell (Fig. 2f). The dependence of MapZ positioning on PG synthesis is further supported by the observation that the extracellular C-terminal domain of MapZ efficiently binds PG (Fig. 2g) and that specific inhibition of PG synthesis using vancomycin led to rapid delocalization of MapZ (Extended Data Fig. 5a).

Δ*mapZ* (Fig. 3a, b), *mapZ*Δ*extra* and *mapZ*Δ*cyto* strains (Extended Data Fig. 5b–e) exhibited severe alterations of FtsZ ring morphology and localization. FtsZ is unable to position at mid-cell (Fig. 3b) and the angles of Z rings with respect to the cell long axis (θ_z) are incorrect, reflecting the inability of FtsZ to find the orthogonal division plan (Fig. 3c). 3D-SIM further revealed major defects of FtsZ structures in the Δ*mapZ* strain (Fig. 3d and compare Supplementary Videos 2 and 3). Aberrant 'non-ring' FtsZ structures are observed in 29% of Δ*mapZ* cells (Fig. 3e). Time-lapse microscopy revealed that FtsZ forms polymers that fail to position correctly and degenerate into aberrant structures, even in cells with as yet normal morphology (Extended Data Fig. 6a and compare Supplementary Videos 4 and 5). PG synthesis colocalized with mispositioned FtsZ (Extended Data Fig. 6b), consequently promoting disorderly cell wall synthesis and leading to morphological defects or cell lysis (Extended Data Fig. 6a and Supplementary Video 5). The remaining 71% of cells had an overrepresentation of abnormally large Z rings (diameter >1,000 nm) and an underrepresentation of Z rings with diameter <800 nm (55% in Δ*mapZ* compared with 75% in wild type) (Fig. 3f). The reduced occurrence of constricting Z rings and the decrease in cells harbouring FtsZ dumbbells (Fig. 3d and Extended Data Fig. 6c) suggest a premature closing of the septal Z ring in Δ*mapZ*. This is further supported by 3D-SIM imaging of 4′,6-diamidino-2-phenylindole (DAPI)-stained nucleoids, which revealed a very dense stretch of DNA trapped at the septum in 19% of Δ*mapZ* division figures (Fig. 3g and Supplementary Video 6). These chromosome pinching events most probably result from the previously inferred premature closing of the septum in an organism that lacks a nucleoid occlusion system[4]. Perhaps less surprisingly, cells with aberrant FtsZ structures also showed aberrant nucleoid shapes (Extended Data Fig. 6d and Supplementary Video 7). Therefore, not only is MapZ required for correct positioning of the Z ring but it is also involved in the regulation of constriction.

Co-immunoprecipitation revealed *in vivo* interaction between FtsZ and MapZ, which is mediated by the cytoplasmic domain of MapZ (Fig. 4a). The cytoplasmic domain of MapZ ($MapZ_{cyto}$) strongly interacts with FtsZ (affinity (K_D) = 8.76 nM), more precisely through its N-terminal peptide, which is predicted to be an α-helix ($MapZ_{(1–41)}$, from Met 1 to Gly 41) (K_D = 20.4 nM) (Extended Data Fig. 7a–d). Other parts of the intracellular domain ($MapZ_{(42–98)}$ and $MapZ_{(42–158)}$) or the extracellular domain ($MapZ_{extra}$) showed no interactions with FtsZ (Extended Data Fig. 7e–g). *In vivo* deletion of the MapZ N-terminal peptide (*mapZ*Δ*(1–41)*) did not impair MapZ septal localization (Extended Data Fig. 6e), but resulted in delocalization of FtsZ (Extended Data Fig. 6f, g), which subsequently leads to aberrant cell morphogenesis, asymmetric division or cell lysis (Extended Data Figs 1a, 6h and Supplementary Video 8). This was also observed in the *mapZ*Δ*cyto* strain (Extended Data Fig. 6i and

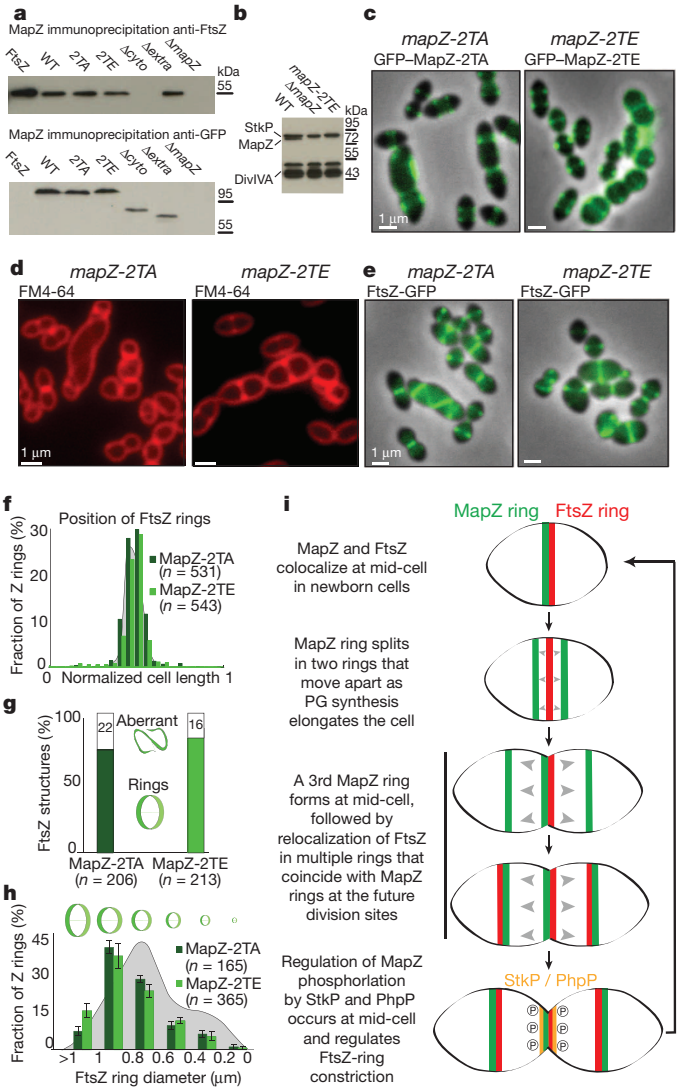


Figure 4 | Characterization of MapZ phosphorylation. **a**, Immunoprecipitation of GFP–MapZ with FtsZ. Anti-FtsZ (top) or anti-GFP (bottom). WT, wild type. **b**, Western blot of cell lysates probed with anti-phosphothreonine antibodies shows phosphorylation signal for MapZ, DivIVA and StkP. **c**, Localization of GFP–MapZ-2TA and GFP–MapZ-2TE. **d**, *mapZ-2TA* and *mapZ-2TE* cells after membrane staining. **e**, Localization of FtsZ–GFP. **f**, Positioning of single FtsZ rings. **g**, Fraction of cells with FtsZ rings or aberrant structures (P value $< 1.54 \times 10^{-10}$ for MapZ-2TA and 1.14×10^{-10} for MapZ-2TE, two-tailed Student's t-test). **h**, Distribution of FtsZ-ring diameters (P value $= 2.9 \times 10^{-4}$ for MapZ-2TA and 9.9×10^{-3} for MapZ-2TE, two-tailed Student's t-test). **i**, Model of MapZ-mediated control of FtsZ positioning (sample of n cells analysed). Images are representative of experiments made in triplicate.

Supplementary Video 9). Therefore, the direct interaction of MapZ with FtsZ is strictly required for FtsZ positioning. Surprisingly, the conserved FtsZ C-terminal tail (Asp 408 to Arg 419), which promotes interaction with FtsZ regulators such as FtsA, EzrA, ZipA and SepF in various bacteria[17–20], is not required for interaction with MapZ (Extended Data Fig. 7h).

In agreement with a previous report[13], we confirmed MapZ phosphorylation by analysing the phosphorylation pattern of MapZ mutants (Fig. 4b). Mass spectrometry analysis of MapZ further showed that MapZ is phosphorylated on Thr 67 and Thr 78 (Extended Data Fig. 8a, b). We then constructed two mutants encoding either the phosphoablative form of MapZ (*mapZ-2TA*) or the phosphomimetic form (*mapZ-2TE*). *mapZ-2TA* and *mapZ-2TE* exhibited cell shape and viability defects (Fig. 4c, d, Extended Data Table 1 and Extended Data Fig. 1a), although

©2014 Macmillan Publishers Limited. All rights reserved

MapZ-2TA and MapZ-2TE retained septal localization (Fig. 4c) and the FtsZ rings were largely well positioned (Fig. 4e, f). Thus, FtsZ positioning by MapZ still occurs properly in *mapZ-2TA* and *mapZ-2TE*, consistent with the observation that phosphorylation does not affect interaction with FtsZ *in vitro* (Fig. 4a and Extended Data Fig. 7i). However, *mapZ-2TA* and *mapZ-2TE* showed aberrant FtsZ structures (Fig. 4g), altered Z-ring diameters (Fig. 4h) and a reduced number of FtsZ rings per cell (Fig. 3g). We conclude that both phosphorylated and dephosphorylated MapZ forms *in vivo*, and that most probably the balance between the two has a role in the control of FtsZ splitting, stability and constriction, but not in positioning.

This work uncovers a novel mechanism in which a single protein has the dual role of marking the cell division site and positioning the FtsZ ring (Fig. 4i). Our data are consistent with a model in which MapZ is anchored at the cell equator by its extracellular domain, which interacts with PG. It is possible that MapZ recognizes a PG structure specific to the mid-cell, such as the equatorial mark visible at the pneumococcal surface (Fig. 1b), reminiscent of the 'piecrust' previously reported in *Staphylococcus aureus*, *S. pneumoniae* and *Enterococcus faecalis*[6,21–23]. As PG synthesis forms the new cell halves, MapZ remains permanently associated with the equators, thus providing a simple mechanism to signal the site of division. MapZ intracellular domains on the inner side of the membrane act as a physical anchor, which positions the FtsZ ring at the division site. Subsequently, MapZ phosphorylation regulates cytokinesis, either through direct regulation of FtsZ or through regulation of other division factors. The fact that MapZ phosphorylation does not occur in the domain that interacts with FtsZ but in the neighbouring one (Extended Data Fig. 7b), and does not affect FtsZ polymerization or GTPase activity (Extended Data Fig. 8c, d), favours the idea of indirect regulation. MapZ cyclic phosphorylation/dephosphorylation most probably occurs when MapZ colocalizes with StkP at mid-cell (Extended Data Fig. 9a) and where the cytoplasmic phosphatase PhpP, which dephosphorylates MapZ (Extended Data Fig. 9b), is enriched[7]. We further hypothesize that MapZ-mediated recruitment of FtsZ is the event that initiates the assembly of the other division proteins at the septum, including GpsB, which has previously been shown[9] to be required for septal positioning of StkP and for the ability of StkP to phosphorylate its targets. Specifically, orchestrated phosphorylation of DivIVA and MapZ enables coordination between PG synthesis and control of the Z ring, respectively.

MapZ is conserved amongst *Streptococcaceae* and most other *Lactobacillales* (Extended Data Fig. 9c). These organisms lack homologues of known FtsZ regulatory systems[2–5]. Thus, the MapZ-mediated mechanism we have uncovered illustrates that pathways of cell division are far more diverse than previously thought in bacteria; they have adapted to the variety of bacterial lifestyles, cell shapes and developmental behaviours.

Online Content Methods, along with any additional Extended Data display items and Source Data, are available in the online version of the paper; references unique to these sections appear only in the online paper.

Received 17 March; accepted 13 October 2014.
Published online 26 November 2014.

1. Adams, D. W. & Errington, J. Bacterial cell division: assembly, maintenance and disassembly of the Z ring. *Nature Rev. Microbiol.* **7,** 642–653 (2009).
2. Bramkamp, M. & van Baarle, S. Division site selection in rod-shaped bacteria. *Curr. Opin. Microbiol.* **12,** 683–688 (2009).
3. Wu, L. J. & Errington, J. Nucleoid occlusion and bacterial cell division. *Nature Rev. Microbiol.* **10,** 8–12 (2012).
4. Pinho, M. G., Kjos, M. & Veening, J. W. How to get (a)round: mechanisms controlling growth and division of coccoid bacteria. *Nature Rev. Microbiol.* **11,** 601–614 (2013).
5. Monahan, L. G. & Harry, E. J. Identifying how bacterial cells find their middle: a new perspective. *Mol. Microbiol.* **87,** 231–234 (2013).
6. Monahan, L. G., Liew, A. T. F., Bottomley, A. L. & Harry, E. J. Division site positioning in bacteria: one size does not fit all. *Front. Microbiol.* **5,** 19 (2014).
7. Beilharz, K. *et al.* Control of cell division in *Streptococcus pneumoniae* by the conserved Ser/Thr protein kinase StkP. *Proc. Natl Acad. Sci. USA* **109,** E905–E913 (2012).
8. Fleurie, A. *et al.* Mutational dissection of the S/T-kinase StkP reveals crucial roles in cell division of *Streptococcus pneumoniae*. *Mol. Microbiol.* **83,** 746–758 (2012).
9. Fleurie, A. *et al.* Interplay of the serine/threonine-kinase StkP and the paralogs DivIVA and GpsB in pneumococcal cell elongation and division. *PLoS Genet.* **10,** e1004275 (2014).
10. Hanks, S. K., Quinn, A. M. & Hunter, T. The protein kinase family: conserved features and deduced phylogeny of the catalytic domains. *Science* **241,** 42–52 (1988).
11. Kannan, N., Taylor, S. S., Zhai, Y., Venter, J. C. & Manning, G. Structural and functional diversity of the microbial kinome. *PLoS Biol.* **5,** e17 (2007).
12. Pereira, S. F., Goss, L. & Dworkin, J. Eukaryote-like serine/threonine kinases and phosphatases in bacteria. *Microbiol. Mol. Biol. Rev.* **75,** 192–212 (2011).
13. Nováková, L. *et al.* Identification of multiple substrates of the StkP Ser/Thr protein kinase in *Streptococcus pneumoniae*. *J. Bacteriol.* **192,** 3629–3638 (2010).
14. Bernsel, A., Viklund, H., Hennerdal, A. & Elofsson, A. TOPCONS: consensus prediction of membrane protein topology. *Nucleic Acids Res.* **37,** W465–W468 (2009).
15. Kuru, E. *et al. In situ* probing of newly synthesized peptidoglycan in live bacteria with fluorescent D-amino acids. *Angew. Chem. Int. Edn Engl.* **51,** 12519–12523 (2012).
16. Daniel, R. A. & Errington, J. Control of cell morphogenesis in bacteria: two distinct ways to make a rod-shaped cell. *Cell* **113,** 767–776 (2003).
17. Ma, X. & Margolin, W. Genetic and functional analyses of the conserved C-terminal core domain of *Escherichia coli* FtsZ. *J. Bacteriol.* **181,** 7531–7544 (1999).
18. Singh, J. K., Makde, R. D., Kumar, V. & Panda, D. A membrane protein, EzrA, regulates assembly dynamics of FtsZ by interacting with the C-terminal tail of FtsZ. *Biochemistry* **46,** 11013–11022 (2007).
19. Haney, S. A. *et al.* Genetic analysis of the *Escherichia coli* FtsZ.ZipA interaction in the yeast two-hybrid system. Characterization of FtsZ residues essential for the interactions with ZipA and with FtsA. *J. Biol. Chem.* **276,** 11980–11987 (2001).
20. Król, E. *et al. Bacillus subtilis* SepF binds to the C-terminus of FtsZ. *PLoS ONE* **7,** e43293 (2012).
21. Wheeler, R., Mesnage, S., Boneca, I. G., Hobbs, J. K. & Foster, S. J. Super-resolution microscopy reveals cell wall dynamics and peptidoglycan architecture in ovococcal bacteria. *Mol. Microbiol.* **82,** 1096–1109 (2011).
22. Tomasz, A., Jamieson, J. D. & Ottolenghi, E. The fine structure of *Diplococcus pneumoniae*. *J. Cell Biol.* **22,** 453–467 (1964).
23. Higgins, M. L. & Shockman, G. D. Model for cell wall growth of *Streptococcus faecalis*. *J. Bacteriol.* **101,** 643–648 (1970).

Supplementary Information is available in the online version of the paper.

Acknowledgements This work was supported by grants from the CNRS, the Université Claude Bernard Lyon 1, the FINOVI foundation, the Agence National de la Recherche (ANR-12-BSV3-0008-01) and the Region Rhône-Alpes (ARC1 and financial support for A.F. (Cluster 10) and C.Z. (CMIRA)). C.L. was supported by a Wellcome Trust Programme Grant to D.S. (WT083469MA), advanced microscopy at Micron Oxford was supported by a Wellcome Trust Strategic Award (091911), and Y.V.B. was supported by a National Institutes of Health grant (GM051986). We acknowledge the contribution of the PLATIM and the Protein Science facilities of the SFR Biosciences Gerland-Lyon Sud (UMS344/US8) and the Centre Technologique des Microstructures de l'Université Lyon 1. We thank C. Chamot for technical assistance in microscopy, S. Uphoff and J. Wiktor for providing help with Matlab and A.-M. Di Guilmi for providing us with the antibody against pneumococcal FtsZ. We thank N. Campo, N. Dubarry and J.-P. Claverys for stimulating discussions and critical reading of the manuscript. N. Campo is also thanked for her help with time-lapse microscopy.

Author Contributions C.G. and C.L. wrote the paper. A.F., C.L., S.M., C.Z., C.Cl., J.-P.L., M.F.-W. and C.G. designed and performed the experiments. C.G., C.L., A.F., S.M., J.-P.L., C.Co., M.F.-W. and B.M. analysed and interpreted the data. E.K., Y.V.B. and M.S.VN. provided new reagents. E.K., Y.B. and D.S. read and commented on the manuscript.

Author Information Reprints and permissions information is available at www.nature.com/reprints. The authors declare no competing financial interests. Readers are welcome to comment on the online version of the paper. Correspondence and requests for materials should be addressed to C.G. (c.grangeasse@ibcp.fr) or C.L. (christian.lesterlin@bioch.ox.ac.uk).

©2014 Macmillan Publishers Limited. All rights reserved

METHODS

Strains, plasmids, primers and growth conditions. *S. pneumoniae* isogenic strains were constructed by transformation in R800 (ref. 8). Standard procedures for chromosomal transformation and growth were used[9,24]. For growth experiments, *S. pneumoniae* strains were cultivated at 37 °C in Todd–Hewitt yeast (THY) broth (Difco). For induction of P_{Zn}, $ZnCl_2$ was added at the concentration of 0.2 mM. For construction of *S. pneumoniae* mutants, transformation was performed as described previously using precompetent cells treated at 37 °C with synthetic competence stimulating peptide 1 (CSP1) to induce competence[8,25]. For viability assays, several samples of exponentially growing cells were taken every 30 min, diluted appropriately and plated onto THY agar supplemented with horse blood. After overnight incubation, colony-forming units (c.f.u.) were counted and the percentage of viability of mutant strains was expressed relative to the wild-type strain. These experiments were biologically made in triplicates. The *Escherichia coli* XL1-Blue strain was used as a host for cloning. *E. coli* BL21(DE3) strain was used as host for overexpression. Strains used in this study are listed in Supplementary Table 1.

Construction of plasmids. DNA fragments coding for full-length MapZ, the extracellular domain, the cytoplasmic domain or peptides of MapZ, the kinase domain of StkP, PhpP and for $FtsZ_{(1–407)}$, were obtained by PCR using chromosomal DNA from *S. pneumoniae* R800 strain as a template and primer pairs 47/48, 39/40, 34/35, 34/36, 37/38, 37/35, 45/46, 41/42 and 43/44, respectively (Supplementary Table 2). DNA fragment coding for the cytoplasmic domain of MapZ with T67-78E mutations was obtained using primer pair 34/35 and the *mapZ-2TE* strain as a template (Supplementary Table 1). $mapZ_{cyto}$, $mapZ_{cyto}$*-2TE*, $mapZ_{(1–41)}$, $mapZ_{(42–98)}$, $mapZ_{(42–158)}$, $mapZ_{extra}$ and *phpP* were cloned between the NdeI and PstI cloning sites of the pT7-7 plasmid[26]. $ftsZ_{(1–407)}$ was cloned between the NdeI and BamHI cloning sites of the pETPhos plasmid[27]. *mapZ* was cloned between the AgeI and NotI cloning sites of the pCM38 plasmid (gift from C. Morlot, see Supplementary Table 1). $stkP_{KD}$ was cloned between the BamHI and HindIII cloning sites of the pQE30 plasmid. The nucleotide sequences of all DNA fragments were checked to ensure error-free amplification.

Allelic replacement mutagenesis. To construct pneumococcus mutants (gene deletions, *gfp/rfp* fusions or site-directed mutagenesis), we used a two-step procedure, based on a bicistronic *kan-rpsL* cassette called Janus[24]. The genes encoding RFP and GFP were from refs 7 and 28, respectively. The Janus procedure allows the replacement of a gene by a cassette and subsequent deletion or substitution of the cassette by a mutated allelic form at the gene chromosomal locus. This procedure avoids polar effects and allows a physiological level of expression of GFP and RFP fusions and mutated proteins. Briefly, the Janus cassette is either used to replace the gene of interest or inserted at either its 5′ or 3′ end. Both options confer resistance to kanamycin and dominant streptomycin sensitivity in the wild-type streptomycin-resistant R800 *rpsL1* strain (Kan^R-Str^S). Then, any DNA fragments flanked on each end by sequences homologous to the upstream and downstream regions of the gene of interest could be used to transform Kan^R-Str^S strains in order to obtain the expected nonpolar markerless mutant strains Kan^S-Str^R. Once obtained, these markerless transformants were re-streaked to single colonies and correct integration at the chromosomal locus was verified by PCR. Full description of primers used for the construction of strains (Supplementary Table 1) is provided in Supplementary Table 2.

Protein purification. Recombinant plasmids overproducing $MapZ_{cyto}$, $MapZ_{cyto}$-T67-78E, $MapZ_{(1–41)}$, $MapZ_{(42–98)}$, $MapZ_{(42–158)}$, $MapZ_{extra}$, $FtsZ_{(1–407)}$, FtsZ, $StkP_{KD}$ and PhpP were transformed into the BL21(DE3) *E. coli* strain. Overexpression and purification of $StkP_{KD}$, and FtsZ and $FtsZ_{(1–407)}$, were performed as previously described in refs 8 and 29, respectively. MapZ wild-type or mutated domains as well as PhpP were purified using the same procedure than $StkP_{KD}$. To purify MapZ from *S. pneumoniae* cells, we used the strain in which *mapZ* is fused to a DNA fragment encoding 6 histidines (Supplementary Table 1) and the procedure was carried out as previously described[9]. We checked that cells grew as the wild-type cells and displayed proper cell shape.

Peptidoglycan labelling with fluorescent D-amino acids. The procedure used was adapted from[15]. Briefly, exponentially growing *gfp-mapZ* or *ftsZ- gfp* strains ($OD_{550\,nm} = 0.1$) were incubated for 1 min at 37 °C in THY with 500 µM of TDL (a fluorescent carboxytetramethylrhodamine derivative of D-alanine). Cells were then washed three times with 1 ml PBS pH 7.4 at room temperature, incubated again for 1 min at 37 °C with 500 µM of HADA (a fluorescent hydroxy coumarin derivative of D-alanine) of $OD_{550\,nm} = 0.1$ and washed three times with PBS. For localization of FtsZ together with PG synthesis, *ΔmapZ ftsZ-gfp* cells were grown up to $OD_{550\,nm} = 0.1$ in THY and labelled for 3 min with 500 µM of TDL, and finally washed three times with PBS. 0.7 µl of each mixture was then placed on slides and observed under the microscope. These experiments were biologically made in triplicates.

Microscopy techniques. Microscopy was performed on exponentially growing cells ($A_{550\,nm} = 0.1$). TEM, SEM, fluorescence and immunofluorescence microscopy were carried out as previously described[8]. Slides were visualized with a Zeiss AxioObserver Z1 microscope fitted with an Orca-R2 C10600 charge-coupled device (CCD) camera (Hamamatsu) with a ×100 NA 1.46 objective. Images were collected with AxioVision (Carl Zeiss). For TEM, cells were examined with a Philips CM120 transmission electron microscope equipped with a Gatan Orius SC200 CCD camera. For SEM, cells were observed with a Quanta 250 FEG (FEI) scanning electron microscope. Time-lapse microscopy was performed as described[30] using an automated inverted epifluorescence microscope Nikon Ti-E/B equipped with the perfect focus system (PFS, Nikon) and a phase contrast objective (CFI Plan Fluor DLL ×100 oil NA 1.3), a Semrock filter set for GFP (Ex: 482BP35; DM: 506; Em: 536BP40), a Nikon Intensilight 130W High-Pressure Mercury Lamp, a monochrome OrcaR2 digital CCD camera (Hamamatsu) and an ImagEM-1K EMCCD camera (Hamamatsu). The microscope is equipped with a chamber thermostated at 30 °C. Images were captured every 5 min and processed using Nis-Elements AR software (Nikon). All fluorescence images were acquired with a minimal exposure time to minimize bleaching and phototoxicity effects. GFP fluorescence images were false coloured green and overlaid on phase contrast images. Super-resolution 3D-SIM imaging was carried out as previously described[31], on a DeltaVision OMX V3 (Applied Precision/GE Healthcare) equipped with a Blaze SIM module, a ×60/1.42 oil UPlanSApo objective (Olympus), 405 nm and 488 nm diode lasers and three sCMOS cameras (PCO). Each 3D-SIM stacks is composed of 225 images (512 × 512 pixels) consisting of 12 z-sections (125 nm z-distance), with 15 images per z-section with the striped illumination pattern[32,33] rotated to the three angles (−60°, 0°, +60°) and shifted in five phase steps. Acquisition settings were as follows: for FtsZ–GFP, 3 ms exposure with 488 nm laser (attenuated to 100% transmission); GFP–MapZ, 7 ms exposure with 488 nm laser (attenuated to 100% transmission); DAPI, 20–30 ms exposure with 405 nm laser (100% transmission). The 3D-SIM raw data was reconstructed with SoftWoRx 6.0 (Applied Precision) using a Wiener filter setting of 0.002 and channel specifically measured optical transfer functions resulting in a lateral (x–y) resolution of 100–130 nm (wavelength dependent) and an axial (z) resolution of ~300. These experiments were technically made in triplicates.

Microscopy image analysis. Snapshot analysis was performed using ImageJ (http://rsb.info.nih.gov/ij/) and the MicrobeTracker suite[34] extended by custom MATLAB routines to generate cell length and width distribution histograms, fluorescent intensity linescans, focus positioning dotplots and histograms, cumulative distributions of cells with 1, 2 and 3 rings, and plots of inter-ring distance (IRD) as a function of cell length. Ring diameter measurements were performed using SoftWoRx 6.0 (Applied Precision). We performed Student's t-tests for statistical analysis of our data using StatPlus plug-in for Excel-Mac (by AnalystSoft), which provided the two-tailed distribution P values given in the figure legends (with a critical value of 0.05). For the cell length distribution analysis presented in Extended Data Fig. 1, a non-parametric statistical analysis was performed, as detailed previously[35,36], to take into account the non-normal distribution of cell sizes in the mutants strains analysed.

Co-immunoprecipitation of FtsZ and GFP–MapZ with anti-GFP antibodies. Cultures of *S. pneumoniae* cells were grown at 37 °C in THY medium until $OD_{550\,nm} = 0.4$. Cell pellets were incubated at 30 °C first for 30 min in buffer A (0.1 mM Tris-HCl, 2 mM $MgCl_2$, 1 M sucrose, 1:100 Protease Inhibitory Cocktail, 1 mg ml^{-1} of DNase I and RNase A) and then in buffer B (0.1 mM Tris-HCl, 1 mM EDTA, 1% (v/v) Triton X-100, 1:100 Protease Inhibitory Cocktail, 1 mg ml^{-1} of DNase I and RNase A) at room temperature for 15 min. After centrifugation, the supernatant was incubated with the GFP-Trap resin suspension according to the manufacturer's instructions (Chromotech). Protein-bound GFP-Trap resins were eluted with Laemmli buffer at 95 °C for 10 min and analysed by SDS–PAGE. These experiments were biologically and technically made in triplicates.

FtsZ polymerization and GTPase assays. FtsZ polymerization assays were performed as described previously[29]. Briefly, mixtures of 3 µM of FtsZ and 6 µM of MapZ, MapZ-2TA or MapZ-2TE were incubated for 15 min at 25 °C in a buffer containing 50 mM HEPES/NaOH, pH 7.2, 50 mM KCl, 10 mM $MgCl_2$ and 1 mM β-mercaptoethanol. Identical reaction conditions were ensured by compensating varying amounts of proteins with the storage buffer. The solutions were subsequently centrifuged for 15 min at 250,000g and 25 °C in a Beckman 50.4 Ti rotor using a Beckmann LE80K ultracentrifuge. After immediate withdrawal of the supernatants, pelleted proteins were dissolved in 150 µl SDS sample buffer and incubated for 10 min at 96 °C. Fifteen microlitres of each sample were then subjected to electrophoresis in a 10% SDS–PAGE gel. For visualization, gels were stained with Brillant Blue R 250 and scanned. These experiments were technically made in triplicates. GTPase assays were performed following the previously described procedure[37]. The reaction was performed in a buffer containing 50 mM HEPES/NaOH pH 7.5 and 300 mM KCl. Master mixes contained 24 µM of FtsZ and when needed 48 µM of $MapZ_{cyto}$ or $MapZ_{cyto}$-2TE.

MapZ *in vitro* phosphorylation and dephosphorylation. *In vitro* phosphorylation of $MapZ_{cyto}$ by $StkP_{KD}$ was carried out by incubating the reaction mixture (200 µl) containing 50 µg of $MapZ_{cyto}$, 1 µg $StkP_{KD}$ and 25 mM Tris-HCl, pH 7.0, 1 mM

©2014 Macmillan Publishers Limited. All rights reserved

dithiothreitol (DTT), 5 mM $MgCl_2$, 1 mM EDTA and 10 μM ATP with 5 μCi [γ-^{32}P]ATP (specific activity 3,000 Ci mmol^{-1}) for 15 min at 37 °C. Twenty microlitres were sampled and mixed with SDS–PAGE loading buffer and heated for 5 min at 100 °C. The remaining mixture was further incubated in the presence of 0.2 μg of purified PhpP and 20 μl aliquots were withdrawn at 30 s, 1, 2, 5, 10 min and mixed with SDS–PAGE loading buffer and heated. After SDS–PAGE analysis, gels were soaked in 16% trichloroacetic acid for 10 min at 90 °C, stained with Coomassie blue, dried and $MapZ_{cyto}$ dephosphorylation was visualized by autoradiography using X-ray films (Kodak BIOMAX-MS). These experiments were technically made in triplicates.

MapZ cell wall binding. Pneumococcal cell wall preparation as well as the procedure used to analyse MapZ binding to the cell wall was described previously[38]. Briefly, 2 μg of purified $MapZ_{extra}$ was incubated with purified *S. pneumoniae* cell wall (5 mg) in 100 μl of a buffer containing 50 mM Tris pH 8.0 and 100 mM NaCl for 16 h at 4 °C. After centrifugation (5 min at 5,000*g*), the supernatant was removed (unbound fraction) and the cell wall pellet was washed three times with PBS (wash fraction) and resuspended in 50 μl SDS–PAGE loading buffer. After incubation at 100 °C for 10 min, the supernatant, corresponding to the cell wall bound to MapZ (bound fraction), was recovered from the cell wall pellet by centrifugation (5 min at 5,000*g*). The different fractions were analysed by SDS–PAGE and western immunoblotting. These experiments were technically made in triplicates.

Immunoblot analysis. *In vivo* phosphorylated proteins in crude extracts of *S. pneumoniae* strains were immunodetected using an anti-phosphothreonine polyclonal antibody (Cell Signaling) at 1/2,000 as described previously[8]. For FtsZ, immunodetection was performed using a specific rabbit polyclonal antibody[39] used at 1/10,000. Detection of GFP fusions was performed using a rabbit anti-GFP antibody (AMS Biotechnology). Detection of $MapZ_{extra}$ in cell wall binding assays was performed using a mouse anti-6×His antibody (Sigma). A goat anti-rabbit secondary antibody horseradish peroxidase (HRP) conjugate (Biorad) was used at 1/5,000 to reveal the immunoblots, except for the cell wall binding assay, in which goat anti-mouse secondary antibody HRP conjugate (Biorad) was used at 1/5,000. These experiments were biologically and technically made in triplicates.

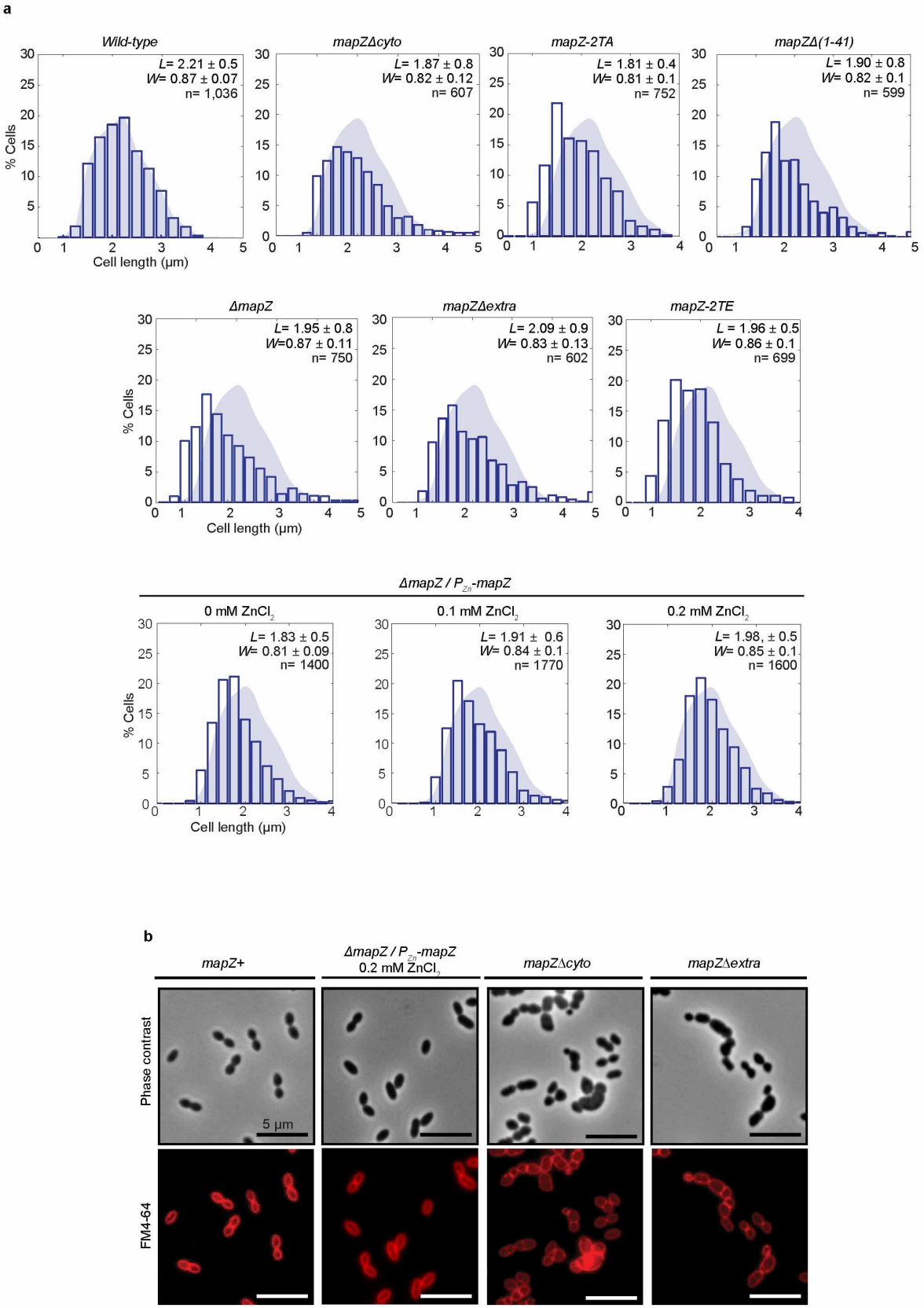
Nano-LC-MS/MS analysis of purified MapZ. Purified MapZ was in gel digested using trypsin as described elsewhere[40]. Peptide mixture was either analysed directly by liquid chromatography coupled to tandem mass spectrometry (LC-MS/MS) after being desalted using C18 StageTips[41] or was subjected to phosphopeptide enrichment by titanium dioxide chromatography as described previously[42] with the following modifications: phosphopeptide elution from the beads was performed three times with 100 ml 40% ammonia hydroxide solution in 60% acetonitrile at a pH of >10.5. Analysis of peptides and phosphopeptides was done on a Proxeon Easy-LC system (Proxeon Biosystems) either coupled to an LTQ-Orbitrap-Elite or to an LTQ-Orbitrap-XL mass spectrometer (Thermo Fisher Scientific) equipped with a nano-electrospray ion source (Proxeon Biosystems) as described previously[43]. The mass spectrometer was operated in the positive ion mode with the following acquisition cycle: one initial full scan in the Orbitrap analyser (MS) was followed by fragmentation through rapid collision induced dissociation (CID) of the 20 most intense multiply charged precursor ions in the linear ion trap analyser (LTQ Elite), or the five most intense precursor ions (LTQ XL). Here multi-stage activation (MSA) was applied in all MS/MS events when a neutral loss event was detected on the precursor ions depending on their charge state: singly (−97.97 Th), doubly (−48.99 Th) and triply (−32.66 Th). Mass spectra were analysed using the software suite MaxQuant, v.1.0.14.3 (ref. 44). The data were searched against a target-decoy *S. pneumoniae* database including the His-tagged sequence of MapZ (35,203 entries) and 262 commonly observed protein contaminants. Trypsin was set as protease and two missed cleavage sites were allowed. Acetylation at the N terminus, oxidation of methionine and phosphorylation on serine, threonine and tyrosine were set as variable modifications. Carbamidomethylation of cysteine was set as fixed modification. Initial precursor mass tolerance was set to 7 p.p.m. at the precursor ion level and 0.5 Da at the fragment ion level. Phosphorylation events with a localization probability of at least 0.75 were considered to be assigned to a specific residue. Spectra of modified peptides were manually validated.

Surface plasmon resonance. Real-time binding experiments were performed on a BIAcore T100 biosensor system (GE Healthcare). FtsZ and $FtsZ_{(1–407)}$ were covalently coupled through its amino groups to the surface of a CM5 sensorchip according to the manufacturer's instructions. Increasing concentrations (0.01, 0.02, 0.05, 0.1, 0.2 and 0.5 μM from bottom to top) of $MapZ_{cyto}$, MapZ(1–41), MapZ(42–98), MapZ(42–158), $MapZ_{extra}$ and $MapZ_{cyto}$-2TE were injected over the surface of the sensorchip at a flow rate of 30 μl min^{-1} in 10 mM HEPES pH 7.4, 150 mM NaCl, 0,005% surfactant P20. For all experiments, non-specific binding to the surface of the sensorchip was subtracted by injection of the analytes over a mocked derivatized sensorchip. The resulting sensorgrams were analysed using BIAevaluation software (GE Healthcare) according to a 1:1 model of interaction to determine the kinetic constants. The goodness of the fit was assessed by inspecting the χ^2 values and the random distribution of the residuals. These experiments were technically made in triplicates.

MapZ sequence analysis and search of MapZ in bacterial genomes. MapZ topology was predicted using TOPSCONS (http://topcons.net)[14] and secondary structure prediction of $MapZ_{cyto}$ was computed using the Network Protein Sequence Analysis (NPSA) (http://npsa-pbil.ibcp.fr) using DSC, PHD and SOPMA methods[45]. MapZ sequences were extracted from UniProtKB[46] complete bacteria genomes by means of GGsearch v.36.3.5c[47] with UniProtKB/Swiss-Prot:Q8DR55 as the query sequence. A multiple sequence alignment was computed with MUSCLE v.3.8.31 (ref. 48) with the 66 extracted sequences. Then, a profile HMM was built with the hmmbuild program of the HMMER 3.0 package[49]. The predicted proteins of the 6,305 bacterial genomes from Ensemble Genomes release[50] were searched with the hmmsearch program and the built profile. Subject sequences were extracted from matches found thanks to an in-house Java program if they observed the following conditions: E value $\leq 1 \times 10^{-24}$ and length between 350 and 650 amino acids.

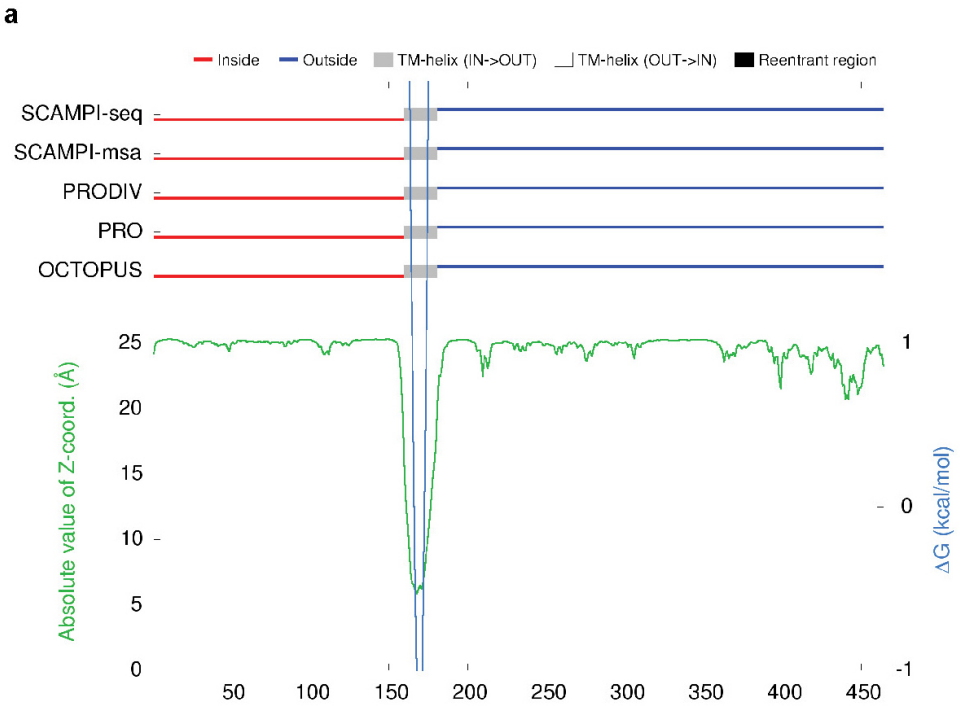
24. Sung, C. K., Li, H., Claverys, J. P. & Morrison, D. A. An *rpsL* cassette, Janus, for gene replacement through negative selection in *Streptococcus pneumoniae*. *Appl. Environ. Microbiol.* **67,** 5190–5196 (2001).
25. Martin, B., Prudhomme, M., Alloing, G., Granadel, C. & Claverys, J. P. Cross-regulation of competence pheromone production and export in the early control of transformation in *Streptococcus pneumoniae*. *Mol. Microbiol.* **38,** 867–878 (2000).
26. Cortay, J. C. *et al. In vitro* asymmetric binding of the pleiotropic regulatory protein, FruR, to the ace operator controlling glyoxylate shunt enzyme synthesis. *J. Biol. Chem.* **269,** 14885–14891 (1994).
27. Canova, M. J., Kremer, L. & Molle, V. pETPhos: a customized expression vector designed for further characterization of Ser/Thr/Tyr protein kinases and their substrates. *Plasmid* **60,** 149–153 (2008).
28. Martin, B. *et al.* Expression and maintenance of ComD–ComE, the two-component signal-transduction system that controls competence of *Streptococcus pneumoniae*. *Mol. Microbiol.* **75,** 1513–1528 (2010).
29. Thanbichler, M. & Shapiro, L. MipZ, a spatial regulator coordinating chromosome segregation with cell division in *Caulobacter*. *Cell* **126,** 147–162 (2006).
30. de Jong, I. G., Beilharz, K., Kuipers, O. P. & Veening, J. W. Live cell imaging of *Bacillus subtilis* and *Streptococcus pneumoniae* using automated time-lapse microscopy. *J. Vis. Exp.* **53,** 3145 (2011).
31. Lesterlin, C., Ball, G., Schermelleh, L. & Sherratt, D. J. RecA bundles mediate homology pairing between distant sisters during DNA break repair. *Nature* **506,** 249–253 (2014).
32. Schermelleh, L. *et al.* Subdiffraction multicolor imaging of the nuclear periphery with 3D structured illumination microscopy. *Science* **320,** 1332–1336 (2008).
33. Gustafsson, M. G. *et al.* Three-dimensional resolution doubling in wide-field fluorescence microscopy by structured illumination. *Biophys. J.* **94,** 4957–4970 (2008).
34. Sliusarenko, O., Heinritz, J., Emonet, T. & Jacobs-Wagner, C. High-throughput, subpixel precision analysis of bacterial morphogenesis and intracellular spatio-temporal dynamics. *Mol. Microbiol.* **80,** 612–627 (2011).
35. Krzywinski, M. & Altman, N. Points of significance: significance, *P* values and *t*-tests. *Nature Methods* **10,** 1041–1042 (2013).
36. Krzywinski, M. & Altman, N. Points of significance: importance of being uncertain. *Nature Methods* **10,** 809–810 (2013).
37. Król, E. & Scheffers, D. J. FtsZ polymerization assays: simple protocols and considerations. *J. Vis. Exp.* **81,** e50844 (2013).
38. Morlot, C. *et al.* Interaction of penicillin-binding protein 2x and Ser/Thr protein kinase StkP, two key players in *Streptococcus pneumoniae* R6 morphogenesis. *Mol. Microbiol.* **90,** 88–102 (2013).
39. Morlot, C., Zapun, A., Dideberg, O. & Vernet, T. Growth and division of *Streptococcus pneumoniae*: localization of the high molecular weight penicillin-binding proteins during the cell cycle. *Mol. Microbiol.* **50,** 845–855 (2003).
40. Borchert, N. *et al.* Proteogenomics of *Pristionchus pacificus* reveals distinct proteome structure of nematode models. *Genome Res.* **20,** 837–846 (2010).
41. Rappsilber, J., Mann, M. & Ishihama, Y. Protocol for micro-purification, enrichment, pre-fractionation and storage of peptides for proteomics using StageTips. *Nature Protocols* **2,** 1896–1906 (2007).
42. Olsen, J. V. *et al.* Parts per million mass accuracy on an Orbitrap mass spectrometer via lock mass injection into a C-trap. *Mol. Cell. Proteomics* **4,** 2010–2021 (2005).
43. Franz-Wachtel, M. *et al.* Global detection of protein kinase D-dependent phosphorylation events in nocodazole-treated human cells. *Mol. Cell. Proteomics* **11,** 160–170 (2012).
44. Cox, J. & Mann, M. MaxQuant enables high peptide identification rates, individualized p.p.b.-range mass accuracies and proteome-wide protein quantification. *Nature Biotechnol.* **26,** 1367–1372 (2008).
45. Combet, C., Blanchet, C., Geourjon, C. & Deleage, G. NPS@: network protein sequence analysis. *Trends Biochem. Sci.* **25,** 147–150 (2000).
46. UniProt Consortium. Update on activities at the Universal Protein Resource (UniProt) in 2013. *Nucleic Acids Res.* **41,** D43–D47 (2013).
47. Pearson, W. R. & Lipman, D. J. Improved tools for biological sequence comparison. *Proc. Natl Acad. Sci. USA* **85,** 2444–2448 (1988).
48. Edgar, R. C. MUSCLE: a multiple sequence alignment method with reduced time and space complexity. *BMC Bioinformatics* **5,** 113 (2004).
49. Eddy, S. R. Accelerated Profile HMM Searches. *PLOS Comput. Biol.* **7,** e1002195 (2011).
50. Flicek, P. *et al.* Ensembl 2013. *Nucleic Acids Res.* **41,** D48–D55 (2013).

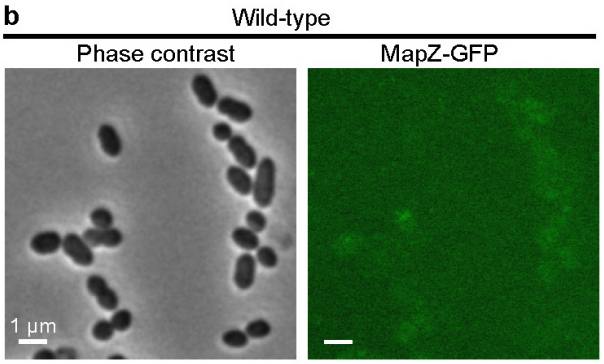
©2014 Macmillan Publishers Limited. All rights reserved



Extended Data Figure 1 | Cell-shape analysis of wild-type and *mapZ* mutant strains. **a**, Cell length distribution of wild-type, Δ*mapZ*, *mapZ-2TA*, *mapZ-2TE*, *mapZΔcyto*, *mapZΔextra* and *mapZΔ(1–41)* strains, as well as for Δ*mapZ*/P_{Zn}-*mapZ* in the presence of 0, 0.1 or 0.2 mM of $ZnCl_2$ inducer. Average cell length (*L*) and width (*W*) are given with standard deviations for a total of *n* cells analysed from three independent experiments. P value $< 1.59 \times 10^{-2}$, two-tailed t distribution determined using a non-parametric statistical test for a critical value of 0.05. **b**, Phase contrast microscopy and FM4-64 membrane staining imaging of $mapZ^+$ cells (*mapZ* is restored at the chromosomal locus in Δ*mapZ*), Δ*mapZ*/P_{Zn}-*mapZ* (Δ*mapZ* cells complemented ectopically with P_{Zn}-*mapZ*), *mapZΔcyto* and *mapZΔextra* cells. Images are representative of experiments made in triplicate.

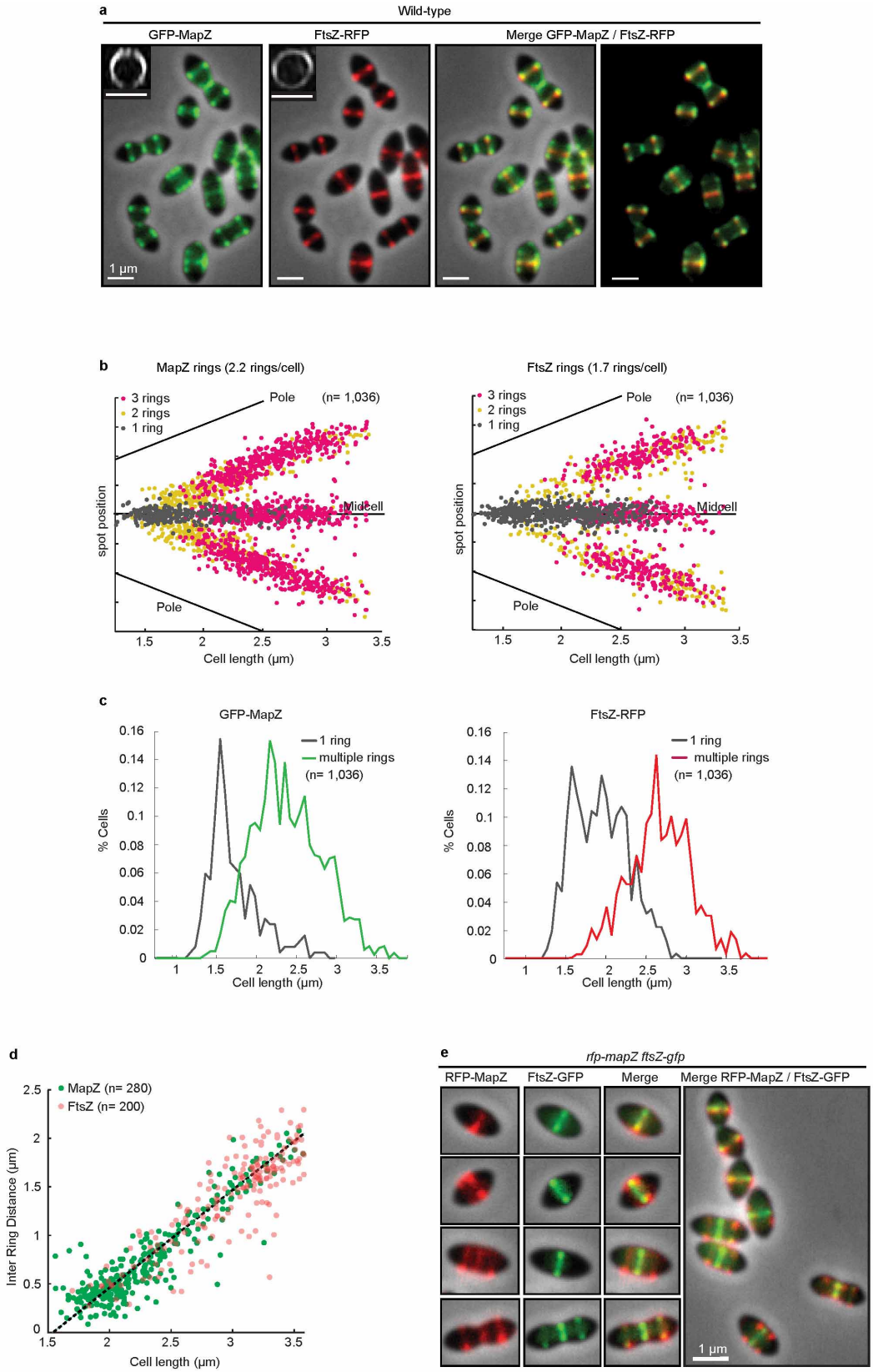
©2014 Macmillan Publishers Limited. All rights reserved





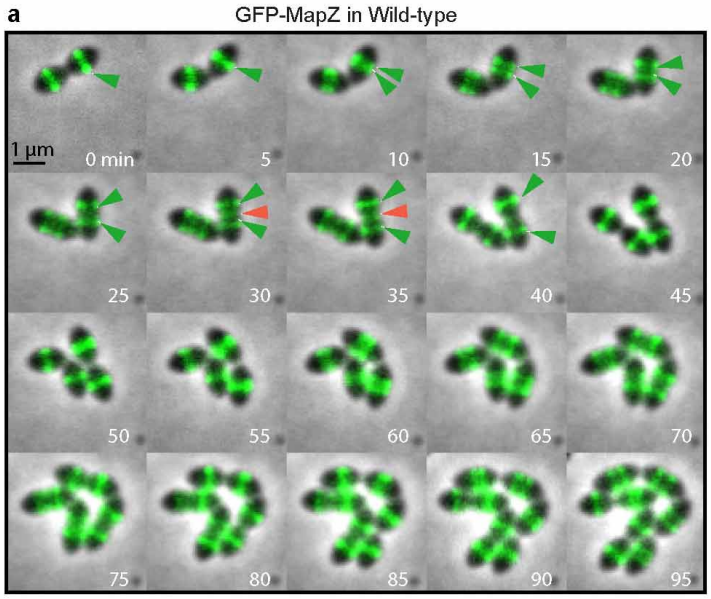
Extended Data Figure 2 | Prediction of MapZ topology. **a**, MapZ topology (that is, specification of the membrane spanning segments and their in/out orientation relative to the membrane) was predicted by five different topology algorithms (SCAMPI-seq, SACAMPI-msa, PRODIV-TMHMM, PRO-TMHMM and OCTOPUS) using TOPCONS (http://topcons.net). ZPRED (green line) predicts the distance to the membrane centre of each amino acid and Δ*G* scale (light blue) shows the predicted free energy of membrane insertion for a window of 21 amino acids centred around each position in the sequence. The transmembrane span is indicated in grey. Predictions of cytoplasmic and extracellular localizations are shown in red and dark blue, respectively. **b**, Wide-field microscopy images of cells producing the C-terminal fusion of MapZ with GFP. GFP fluorescence (right panel) and phase contrast images (left panel). Images are representative of experiments made in triplicate.

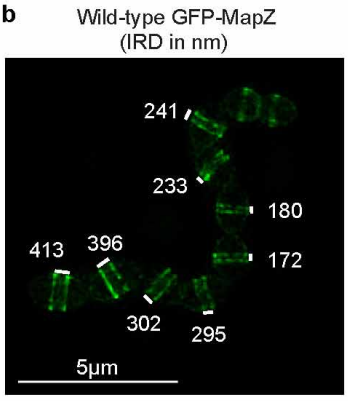
©2014 Macmillan Publishers Limited. All rights reserved

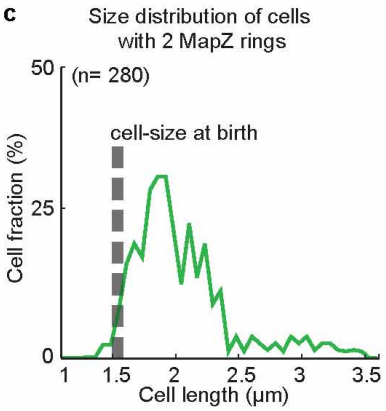


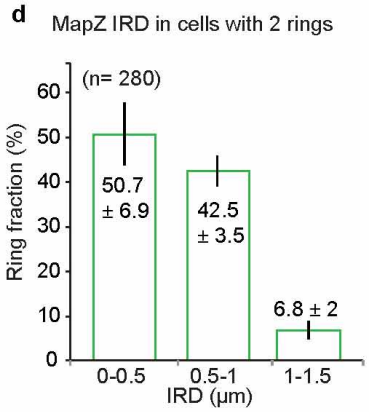
Extended Data Figure 3 | Localization of MapZ and FtsZ in wild-type cells. **a**, Microscopy images of GFP–MapZ and FtsZ–RFP in wild-type cells. Insert images show 3D-SIM orthogonal views of MapZ and FtsZ rings. **b**, Localization dotplots of MapZ-ring and FtsZ-ring positions along the cell length in wild-type cells. **c**, Ratio of cells with single or multiple MapZ rings and FtsZ rings as a function of cell length. **b**, **c**, Data are derived from analysis of 1,036 cells (*n* indicates the number of cells analysed in each panel). **d**, Distance between MapZ outer rings compared with distance between FtsZ outer rings as a function of cell length. **e**, Same as Fig. 2b but after swapping the GFP and RFP fluorescent protein labels. Indicative images showing MapZ, FtsZ, or both MapZ and FtsZ signals are shown for *rfp-mapZ ftsZ-gfp* cells at four different cell cycle stages. A wide-field view is also shown. Images are representative of experiments made in triplicate.

©2014 Macmillan Publishers Limited. All rights reserved



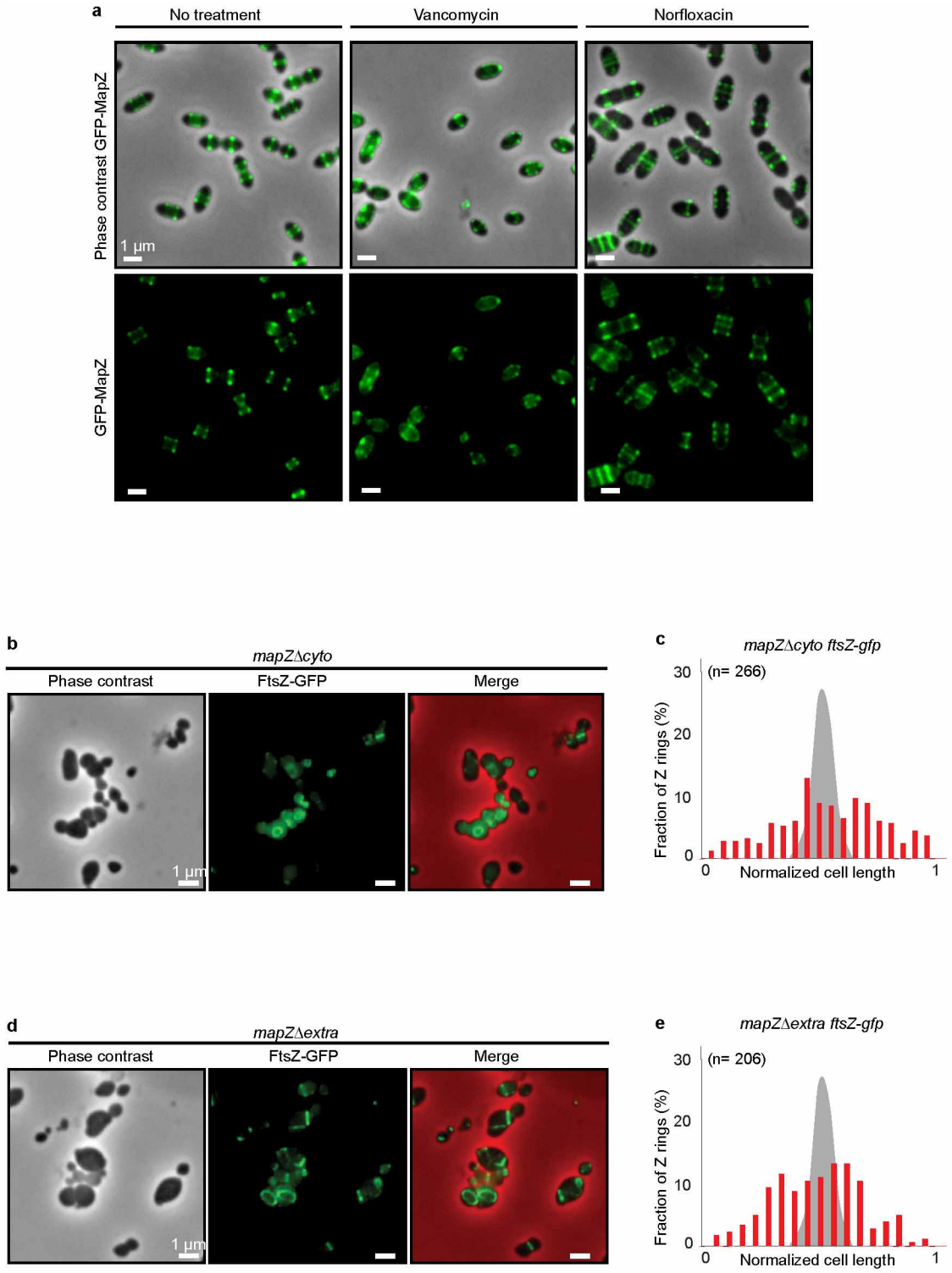






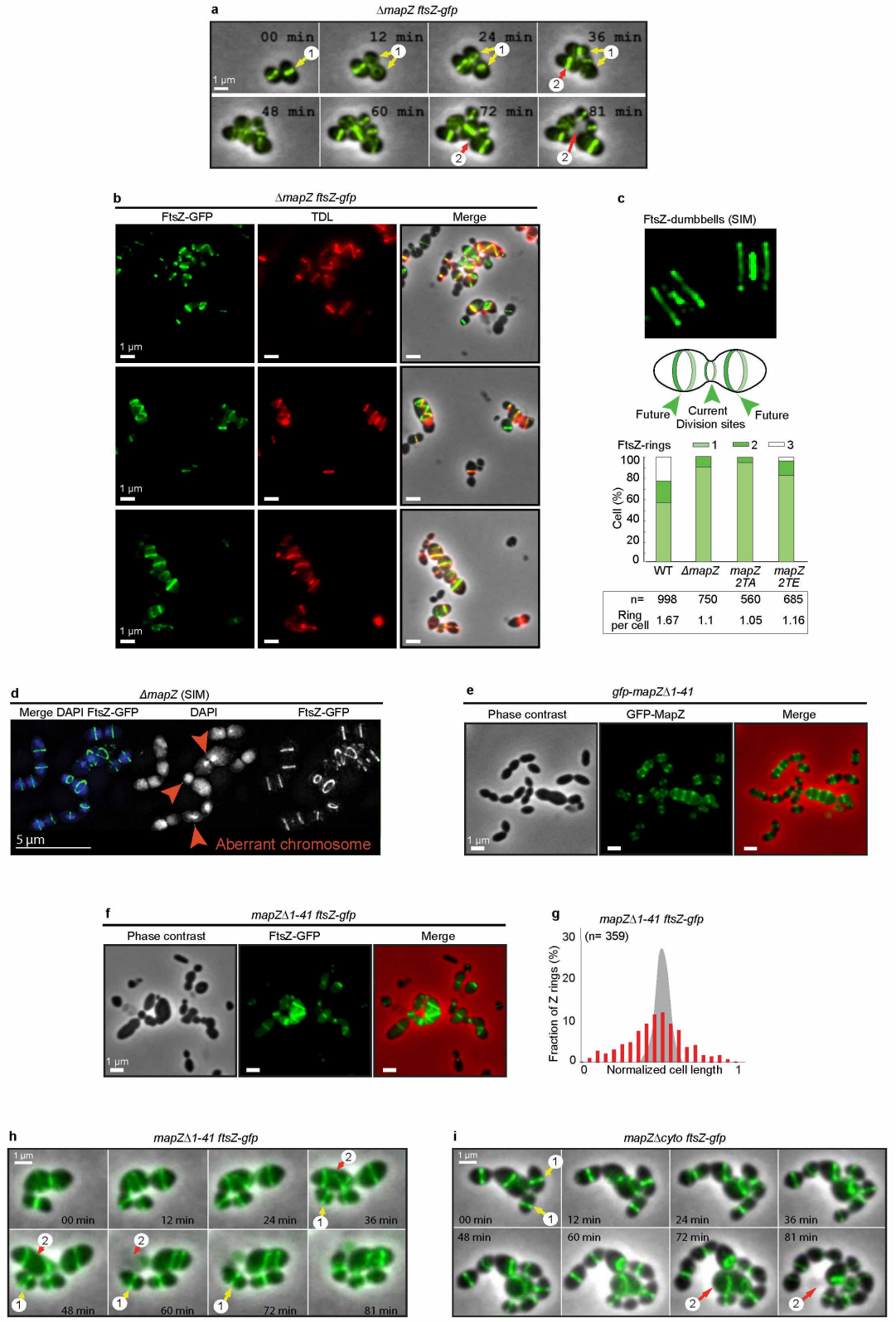
Extended Data Figure 4 | Early splitting of MapZ rings during elongation of wild-type cells. **a**, Time-lapse images of GFP–MapZ dynamics during cell growth and division showing progressive separation of the outer rings (green arrow) and appearance of a 3rd mid-cell ring (red arrow) (similar to Supplementary Video 1). Time is given in minutes. **b**, 3D-SIM images showing the very early stages of MapZ separation in the first stages of cell elongation. The numbers correspond to the inter-ring distance (IRD) in nm. **c**, Cell size distribution of cells with two MapZ rings reveals splitting of MapZ in the early stages of cells elongation. **d**, Distribution of IRD in cells with two MapZ rings (error bars show s.d. from three experiments). **c**, **d**, Data are derived from analysis of 280 cells (*n* indicates the number of cells analysed in each panel). Images are representative of experiments made in triplicate.

©2014 Macmillan Publishers Limited. All rights reserved



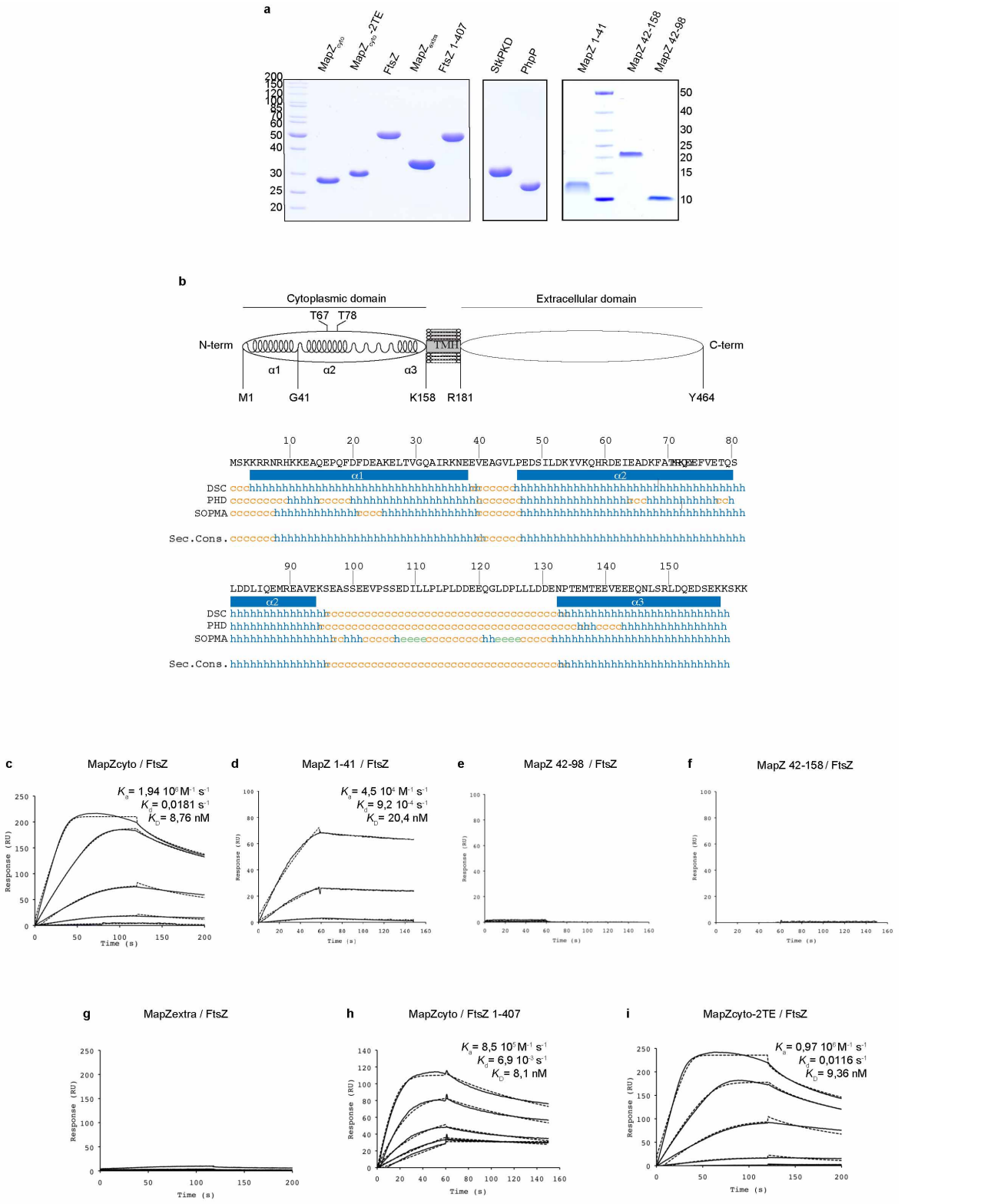
Extended Data Figure 5 | MapZ position depends on PG synthesis and FtsZ position depends on MapZ functionality. **a**, Localization of MapZ after inhibition of PG synthesis in wild-type pneumococcus. Microscopy images of GFP–MapZ in wild-type cells before (top), and 15 min after addition of vancomycin (middle) or norfloxacin (bottom). Vancomycin, which inhibits PG synthesis, impairs localization of GFP–MapZ, whereas norfloxacin, which inhibits topoisomerases, has no effect on MapZ septal localization. **b**, **c**, Localization of FtsZ–GFP in *mapZΔcyto* (**b**) and corresponding FtsZ–GFP ring positioning along the cell length normalized to 1 (**c**). **d**, **e**, Localization of FtsZ–GFP in *mapZΔextra* (**d**) and corresponding FtsZ–GFP ring positioning along the cell length normalized to 1 (**e**). Images are representative of experiments made in triplicate.

©2014 Macmillan Publishers Limited. All rights reserved



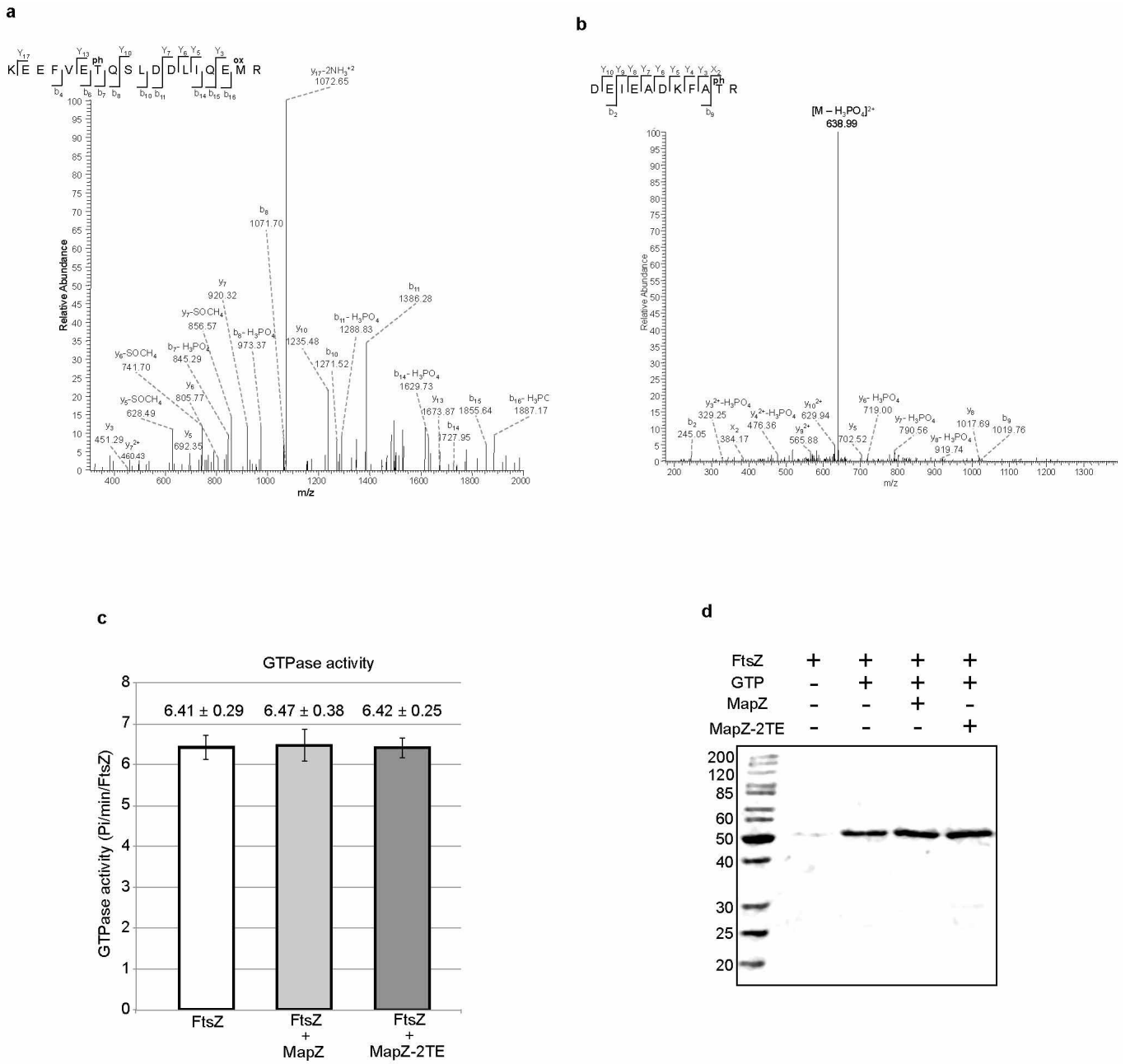
Extended Data Figure 6 | FtsZ is mispositioned in Δ*mapZ* cells and colocalizes with PG synthesis. **a**, Time-lapse images of FtsZ–GFP (green) dynamics in Δ*mapZ* cells. FtsZ polymers fail to position correctly even in cells with normal shape (arrow 1), resulting in asymmetric cell division or cell lysis (arrow 2) (stills correspond to Supplementary Video 5). **b**, Microscopy images showing colocalization of PG synthesis revealed by pulse labelling with TDL (red) and mispositioned FtsZ–GFP structures (green) in Δ*mapZ* cells. Three fields of view from three independent experiments are shown. **c**, 3D-SIM and schematic of FtsZ dumbbells with histograms of the cell ratios with 1, 2 or 3 rings. The average number of rings per cell is shown. **d**, 3D-SIM image of DAPI-stained DNA and FtsZ–GFP in Δ*mapZ* cells. **e**, Localization of GFP–MapZΔ(1–41) in *gfp-mapZΔ(1–41)*. **f**, Localization of FtsZ–GFP in *mapZΔ(1–41)*. **g**, Corresponding FtsZ–GFP ring positioning along the cell length normalized to 1. **h**, **i**, Time-lapse images of FtsZ–GFP (green) dynamics in *mapZΔ(1–41)* (**h**) and *mapZΔcyto* (**i**) cells. FtsZ mispositioning, even in cells with normal shape leads to asymmetric cell division (arrow 1) or cell lysis (arrow 2). Images are representative of experiments made in triplicate.

©2014 Macmillan Publishers Limited. All rights reserved



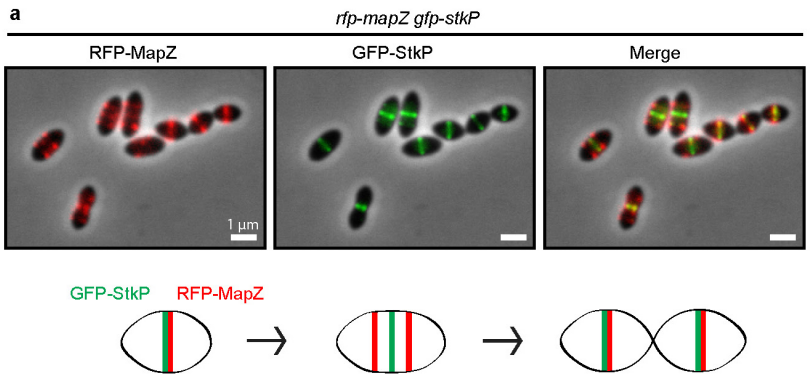
Extended Data Figure 7 | Purification of FtsZ and MapZ and analysis of the interactions between them. **a**, Purification of proteins used in surface plasmon resonance experiments. The MapZ cytoplasmic domain, MapZ-2TE cytoplasmic domain, FtsZ, MapZ extracellular domain, $FtsZ_{(1–407)}$ fragment (FtsZ deleted from the C-terminal α-helix), StkP cytoplasmic domain, PhpP, MapZ N-terminal peptide from Met 1 to Gly 41, MapZ peptide from Val 42 to Ser 98 and MapZ peptide from Val 42 to Lys 158 were overproduced in *E. coli* BL21 and analysed by SDS–PAGE. **b**, Schematic model of MapZ and secondary structure prediction of the cytoplasmic domain of MapZ. Secondary structure codes 'e', 'c' and 'h' indicate predicted α-helices (blue), random coils (orange) and extended strands (green), respectively. **c**–**e**, Surface plasmon resonance analyses of interaction between FtsZ and MapZ. **c**–**i**, Full-length FtsZ (**c**, **d**, **e**, **f**, **g**, **i**) or $FtsZ_{1-407}$ (**h**) was covalently coupled to the surface of a CM5 sensorchip. Increasing amounts of either MapZ cytoplasmic domain (**c**, **h**), MapZ extracellular domain (**g**), MapZ-2TE (**i**) cytoplasmic domain, MapZ(1–41) (**d**), MapZ(42–98) (**e**) and MapZ(42–158) (**f**) peptides were injected onto the FtsZ- or $FtsZ_{(1–407)}$-coupled sensorship. RU, resonance units. The measurements were made in triplicate. The affinity (K_D), association (K_a) and dissociation constants (K_d) are indicated. Images are representative of experiments made in triplicate.

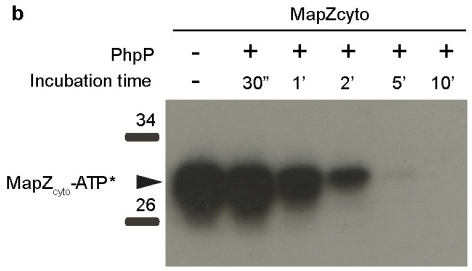
©2014 Macmillan Publishers Limited. All rights reserved



Extended Data Figure 8 | Analysis of MapZ *in vivo* phosphorylation and impact on FtsZ GTPase activity and polymerization. **a**, **b**, MapZ is phosphorylated on threonine 67 (**a**) and threonine 78 (**b**). The spectra show the fragmentation pattern of the phosphopeptides DEIEADKFAT(ph)R corresponding to amino acids 58–68 and KEEFVET(ph)QSLDDLIQEM(ox)R corresponding to amino acids 72–89. **c**, Influence of MapZ and MapZ-2TE cytoplasmic domains on FtsZ GTPase activity. Purified FtsZ was incubated with GTP either alone or in the presence of MapZ or MapZ-2TE cytoplasmic domains and free phosphate was revealed using malachite green colour development. Data are shown with s.d. for three independent experiments. **d**, FtsZ polymerization in the presence of $MapZ_{cyto}$, wild-type or mutated, cytoplasmic domains. FtsZ was incubated in the presence or absence of GTP and either MapZ or MapZ-2TE. The samples were then processed as described in Methods. Images are representative of experiments made in triplicate.

©2014 Macmillan Publishers Limited. All rights reserved





c

Bacterial Genus (#)*	Sequenced genomes (#)	Genomes with MapZ homologues (#)	(%)*
Bacteria	861	6,305	483	7.66
Other	740	4,629	0	0.00
Firmicutes	121	1,676	483	28.82
Other	83	330	0	0.00
Bacillales	23	567	1	0.18
Other	14	359	0	0.00
Bacillaceae	9	208	1	0.48
Other	8	20	0	0.00
Bacillus	1	188	1	0.53
Lactobacillales	15	779	482	61.87
Other	9	186	0	0.00
Enterococcaceae	4	169	70	41.42
Other	2	2	0	0.00
Enterococcus	1	165	68	41.21
Melissococcus	1	2	2	100.00
Streptococcaceae	2	424	412	97.17
Lactococcus	1	14	14	100.00
Streptococcus	1	410	398	97.07

* # for numbers and % for fractions

Extended Data Figure 9 | Interplay between MapZ and StkP and PhpP and conservation of MaZ in bacterial genomes. **a**, Simultaneous localization of GFP–StkP and RFP–MapZ in wild-type cells. Overlays between GFP (green), RFP (red) and phase contrast show that StkP locates at mid-cell while MapZ ring separation proceeds, as depicted in the summary diagram below. **b**, Dephosphorylation of MapZ by PhpP. MapZ cytoplasmic domain was phosphorylated by $StkP_{KD}$ and then incubated for various times (30 s to 10 min) with the protein phosphatase PhpP. MapZ dephosphorylation was analysed by autoradiography. **c**, Conservation analysis of *mapZ* homologues in 6,305 bacterial genomes. The left panel shows the taxonomy of the bacterial superkingdom. The right panel indicates the number of genera, the number of sequenced genomes, the number of genomes coding for MapZ homologous proteins and the percentage of genomes coding for MapZ homologous proteins. Images are representative of experiments made in triplicate.

©2014 Macmillan Publishers Limited. All rights reserved

Extended Data Table 1 | Strain viability and generation time

Strains	Viability[a] (%)	Generation time[b] (min)
WT	100	32 ± 3
ΔmapZ	70.3 ± 0,7	48 ± 2
mapZ-2TA	87 ± 2,7	31 ± 3
mapZ-2TE	95.8 ± 2,9	33 ± 2
mapZ+	97.9±1.1	35±2
ΔmapZ / Pzn-mapZ (no $ZnCl_2$)	78.6 ± 1.2	40± 2
ΔmapZ / Pzn-mapZ (0.1 mM $ZnCl_2$)	84 ± 2.1	39± 3
ΔmapZ / Pzn-mapZ (0.2 mM $ZnCl_2$)	89.5 ± 1.3	34.8 ±2
ftsZ-gfp	96.9 ± 4,3	34 ± 6
gfp-mapZ	95 ± 5	28 ± 3
mapZΔcyto	73.4 ± 2,7	46 ± 3
mapZΔ(1-41)	80.4± 1.3	36 ± 3
mapZΔextra	73.7 ± 0,8	49 ± 5

* Colony-forming units per millilitre (c.f.u. ml^{-1}) estimated by plating and normalized to that of wild-type strain. Data are shown with s.d. for three independent experiments.
† Time required for doubling of the optical density ($OD_{650\,nm}$) in liquid culture. Data are shown with s.d. for three independent experiments.

©2014 Macmillan Publishers Limited. All rights reserved